1 **Supplementary Information (Data Repository [DR1])**

2 **1.1 Near-source Tephrostratigraphy and Tephra Correlations (Volcanic Glass**
3 **chemistry)**

4 The 87.5m long S-19 borehole (40.883 Lat; 14.251 Long; 93m altitude) was drilled ~ 5 km
5 NE of the Campanian Ignimbrite (CI) caldera rim (Fig. 1B). The sequence preserves
6 pyroclastic deposits of numerous eruptions, which are interlayered between palaeosols,
7 peat, marine sediments, along with reworked continental deposits. The deposits of the
8 Neapolitan Yellow Tuff (NYT) are found at 15.5 m below the ground surface, while the top of
9 the CI was encountered at a depth of ~ 29.5 m. There are 6 primary tephra units in the 14
10 meter succession from the Tufi Biancastri sequence. The primary pyroclastic deposits vary
11 in thickness from a few cm to more than 3 m. The thickest tephra is the third primary unit (3)
12 above the CI deposit, it is 3.4 meters thick and spans 25.9 to 22.5 meters (Fig. 2). The basal
13 part of this deposit is composed of 5 cm of well sorted, yellow/orange coloured fine ash, and
14 overlying this is well-stratified, millimetre to centimetre thick stratifications of millimetre sized
15 pumice fragments that are light grey in colour. This 5 cm sub-unit is separated from the
16 overlying thicker portion of the deposit by a sharp planar contact. The upper sub-unit is a
17 grey to light-grey, fine-medium to coarse ash deposit with abundant large (up to 2.5 cm in
18 diameter) accretionary lapilli, and millimetre to a few centimetre-sized angular grey pumices
19 that are porphyritic with biotite and pyroxene crystals and minor feldspar. Sometimes the
20 pumice fragments are characterized by elongated vesicles, and occasionally the pumices
21 are concentrated in thin levels. This upper sub-unit of Unit 3 (3.3 meters) in S-19 is
22 interpreted as a pyroclastic density current (PDC) deposit.

23 Overlying the CI at the investigated Ponte Rossi (PR) outcrop (40.877 Lat; 14.265 Long;
24 60m altitude) were eight eruption units interbedded with paleosols, representing eruption
25 hiatuses at the site, allowing periods of soil formation (Fig. S1). The fourth unit above the CI
26 is the thickest in the Ponti Rossi succession, totalling 90 cm (Fig. S1). It rests on a thin,
27 poorly developed paleosol (evidence of humification), which caps a 10 cm thick, poorly
28 sorted fine-to coarse ash unit (Sample CF129). The basal 10 cm of PR eruption Unit 4
29 comprises well-stratified millimetre to centimetre sized, moderately sorted, fine to medium
30 pumice lapilli fall with occasional lithics (sample CF131; Fig. S1). Following a sharp contact,
31 there is 30 cm of moderately well-sorted fine ash that gradually transitions into 20 cm of
32 poorly sorted ash and pumice lapilli, with pumice lapilli up to 7 cm in diameter. This unit also
33 contains abundant accretionary lapilli with pumice fragments as cores, and are up to 2.5 cm
34 in diameter. The upper portion of Ponti Rossi Unit 4 comprises of 30 cm of poorly sorted, fine
35 to coarse ash (sample CF132), and this is interpreted as a PDC deposit.

36 The deposit characteristic of the post-CI S-19 Unit 3 and the Ponti Rossi Unit 4 show a large
37 degree of similarity supporting their stratigraphic correlation. Indeed both these eruption
38 units are the thickest deposits in their respective post-CI stratigraphic successions and
39 contain large accretionary lapilli, which are not observed in any of the other Tufi Biancastri
40 units.

41 Major and trace element volcanic glass chemistry were used to establish the stratigraphic
42 correlations of tephra units in the Ponti Rossi (SFig. 1) and S-19 borehole Tufi Biancastri
43 sequences, and their correlation to the distal Y-3 tephrostratigraphic marker (Albert et al.,
44 2015). Grain-specific glass chemical analysis was carried out on individual pumice and ash

45   grains from the near-source deposits. Major and minor elements were determined using a
46   wavelength-dispersive JEOL 8600 electron micro-probe (EMP) at the University of Oxford,
47   with an electron beam accelerating voltage of 15kV was used with a 6nA current with a
48   beam diameter of 10 μm following the methods and data accuracies reported in Smith et al.
49   (2011). Accuracies were monitored using reference glasses (ATHO-G, StHs6/80 and
50   GOR132) from MPI-DING (Jochum et al., 2006) and are these analyses are provided in the
51   **Data Repository 2**.

52   Trace element analysis was determined using laser ablation inductively coupled plasma
53   mass spectrometry (LA-ICP-MS), with a Thermo Scientific iCAP Qc ICP-MS coupled to a
54   Teledyne Photon Machines Analyte G2 193 nm eximer laser ablation system with a HelEx II
55   two-volume ablation cell at Trinity College, Dublin. The trace element analyses were carried
56   out using a 25 μm spot, the laser repetition rate was 5 Hz and the count time was 40 s (200
57   pulses) on the sample and 40 s on the gas blank (background). The ablated sample was
58   transported in He gas flow (0.65 L min^{-1}) with additional N_2 (5 ml min^{-1}) via a signal
59   smoothing device. Concentrations were calibrated using NIST612 with ^{29}Si as the internal
60   standard, where EPMA data reveals mingled clasts/shards the appropriate ^{29}Si value was
61   used by comparing the ^{44}Ca concentration measured using the LA-ICP-MS with those of the
62   EPMA. Data reduction was performed using Iolite 2.5 and portions of the signal
63   compromised by the ablation of microcrysts and resin-filled voids were excluded. Accuracies
64   of reference glasses (ATHO-G and StHs6/80-G MPI-DING; Jochum et al., 2006) are typically
65   ≤5% for all elements. Full glass chemical data sets for the Masseria del Monte Tuff (Ponti
66   Rossi samples CF131/132 and S-19 (25.9-22.5m) are presented in **Data Repository 2**,
67   along with secondary standards run alongside the unknown tephra deposits, and those from
68   Albert et al., (2015).

69   Representative analyses of the Ponti Rossi (CF 131/132) and S-19 (25.8m/22.9m) tephra
70   are provided here in **Table S1,** along with that of the type locality Y-3 tephra in the Ionian
71   Sea. Tephra correlations were verified by a range of diagnostic major and trace element bi-
72   plots as defined in Albert et al. (2015) (**Fig. S2**). The thin ash fall unit at Ponti Rossi
73   underlying the Masseria del Monte Tuff/Y-3 eruption deposit, the third unit above the CI also
74   contains the diagnostic bi-modal major element phono-trachytic and trachytic components (1
75   and 2) consistent with the distal Y-3 tephra, however trace element data indicate that this
76   unit is characterised by higher levels of incompatible trace element enrichment, this in
77   conjunction with its limited thickness allow us to exclude it as the near-source equivalent of
78   the widespread Y-3 tephra (**Fig. S2**). The possibility that by combining the compositions of
79   two eruption deposits, such as CF128, and CF129, to satisfy the overall compositional
80   variability of the distal Y-3 tephra is not possible as they are separated by a well-developed
81   palaesol, temporal hiatuses allowing such soil formation (hundreds to thousands of years)
82   would have resulted in separate layers in some of the higher resolution sedimentary records
83   of the Mediterranean region (e.g., Lago Grande di Monticchio).

84   **1.2 Geochronology ^{40}Ar/^{39}Ar Geochronology (LSCE-BGC):**

85   ^{40}Ar/^{39}Ar geochronology was performed on pristine sanidine crystals from three near-source
86   pyroclastic samples, one sample was analysed at Laboratoire des Science du Climat et de
87   l'Environment (CNRS-LSCE; Gif Su Yvette, France) and a further two samples were
88   analysed at the Berkeley Geochronology Center (BGC; Berkeley, USA). Weighted mean
89   ages of both the LSCE and BGC dates are calibrated to the age of the Alder Creek Sanidine

90 (ACs) =1.1891 ± 0.0008 Ma (1σ, Niespolo et al., 2017) and the decay constants of Renne et
91 al (2011).

1.2.1 CNRS-LSCE

93 Sanidine crystals from tephra sample S-19-22.9m were sieved and washed in water. Clear
94 and unaltered sanidine crystals ranging from 250 μm up to 1 mm in size were handpicked
95 under a binocular microscope. To prevent any groundmass contamination, crystals were
96 leached for 5 min in dilute (5 to 7%) hydrofluoric acid. Approximately 40 crystals were then
97 chosen and loaded separately in aluminium disks in order to obtain ages on single-grains
98 (N1530-01 to 17) or on small populations (2 to 3 crystals, N1539-01 to 07) when the grains
99 were to small to be measured individually. Samples were then irradiated for 45 min (IRR
100 119, J value = 3,6070. 10-4) in the β1 tube of the OSIRIS reactor (French Atomic Energy
101 Commission, Saclay, France). After irradiation, samples were transferred into a copper
102 holder and crystals were loaded in individual holes. This copper holder was then placed into
103 a differential vacuum Cleartran$^{©}$ window. Sanidines were then fused using a Synrad CO_2
104 laser (ca. 25 Watts) and the relative quantities of the argon isotopes (^{40}Ar, ^{39}Ar, ^{38}Ar, ^{37}Ar and
105 ^{36}Ar) were measured using a VG 5400 mass spectrometer equipped with a single ion
106 counter (Balzers SEV 217 SEN). Each Ar isotope measurement consisted of 20 cycles of
107 peak switching of the argon isotopes. J values were obtained by co-irradiation of the Alder
108 Creek sanidine standard (ACs-2 at 1.1891 ± 0.0008 Ma (1σ); Niespolo et al., 2017; Renne et
109 al., 2011) placed in the same pit as the samples during irradiation. Mass discrimination was
110 assessed by analysis of air pipette throughout the analytical period, and was calculated
111 relative to a $^{40}Ar/^{36}Ar$ ratio of 298.56 (Lee et al., 2006). Procedural blanks were measured
112 every two or three unknown measurements. For a typical 10 min static blank, the
113 backgrounds were generally about 3.0–4.0 × 10^{-17} and 6.0–7.0 × 10^{-19} mol for ^{40}Ar and ^{36}Ar,
114 respectively. The nucleogenic production ratios used to correct for reactor-produced Ar
115 isotopes from K and Ca are reported in the **Data Repository 3**.

1.2.2 BGC

117 Sanidine from tephra samples S-19-25.8m and Ponti Rossi CF132 were sieved and washed
118 in distilled water in an ultrasonic bath. Sanidine grains were separated using a Frantz
119 Isodynamic magnetic separator and heavy liquids. S-19 tephra sample 25.8 was rinsed in
120 dilute HF for one minute. All samples were finally handpicked to purity. Sanidine crystals
121 from S-19-25.8m and from Ponti Rossi CF132 were loaded into a sixteen-pit 18.5-mm
122 aluminium disk: samples were placed into large 4.5- mm diameter; Alder Creek sanidine
123 (ACs) crystals were loaded into surrounding 3.18-mm pits as a neutron fluence monitor
124 (Nomade et al., 2005). The disk was irradiated for 1 hour at the Cd-lined, in-core CLICIT
125 facility of the Oregon State University TRIGA reactor and labelled irradiation 457PRA. J-
126 values of samples were determined by interpolation of a planar fit to J-values determined
127 from the ACs fluence monitor using the optimization age of 1.1891 ± 0.0008 Ma (1σ)
128 (Niespolo et al., 2017; Renne et al., 2011).

129 Sanidine crystals from S-19-25.8 and Ponti Rossi CF132, and ACs standards, were
130 analysed on a MAP 215-50 mass spectrometer, dubbed Nexus, with a Nier-type ion source
131 and an analogue electron multiplier detector. Single grains of the samples underwent total
132 laser fusion from a CO_2 laser at 7 Watts of power. ACs samples from small pits were
133 measured by total fusion of 3-grain aliquots. For each sample, blank and air pipette, fifteen

134 cycles at 8-35 integrations per cycle were determined for each Ar isotope using peak
135 hopping by magnetic field switching on a single detector. Evolved gases were cooled to ca. -
136 130 to -135 $^\circ$C using a cryotrap and exposed to a c. 450 $^\circ$C hot getter to remove reactive
137 gases. For all samples, a mean blank correction was determined using background isotopic
138 measurements analysed between each single-grain analysis. Blanks between sample
139 measurements were stationary over time, and mean values and standard deviations were
140 used to correct the sample and air pipette data. Mass discrimination was determined based
141 on automated analyses of air pipettes between every five single grain analyses (plus
142 intercalated blanks) using air pipette data based on a power law correction (Renne et al.,
143 2009) and the atmospheric values of Lee et al. (2006). See the **Data Repository 3** for mass
144 discrimination values.

145 Ar isotopic measurements of sanidine crystals from Ponti Rossi CF132 and ACs standards
146 were also analysed on a *Noblesse* 5-collector sector-magnet mass spectrometer, configured
147 with one axial Faraday detector and four off-axis, symmetrically arrayed ETP ion counters.
148 Quasi-uniform heating of each sample (a single grain of sanidine) was achieved via
149 illumination with a CO_2 laser fitted with a beam-shaping lens to generate a flat energy profile
150 of adjustable diameter, typically 2 mm at the target distance. Individual grains of ACs
151 sanidine were heated for ~30 seconds at progressively increasing power levels (1.5–8 watts)
152 until fusion was achieved, typically in 3-4 steps. Evolved gas was exposed for several
153 minutes to an approximately -130°C cryotrap to remove H_2O, and to a GP-50 SAES getter to
154 remove reactive gases. Integrated ages of the step-heating results of ACs were used to
155 calculate J values and provide the basis for liner interpolation of J values for unknowns.
156 Single grains of CF132 were totally fused at 8-9 watts. Five Ar isotopes were measured, with
157 simultaneous measurement of ^{40}Ar, ^{37}Ar, and ^{36}Ar on separate ion counters over a period of
158 ~800 seconds, alternating with peak hopping to position ^{38}Ar and ^{39}Ar on the same ion
159 counter as ^{40}Ar. All signals were normalized to the ^{40}Ar ion counter. ^{36}Ar signal normalization
160 was achieved through periodic measurement of the ^{40}Ar/^{36}Ar ratio of air argon (Lee et al.,
161 2006) inlet from an air-reservoir pipetting system. ^{37}Ar and ^{38}Ar signal normalizations were
162 achieved through periodic measurement of ^{40}Ar from a static gas sample on relevant
163 detectors in a round-robin peak-hopping procedure. Procedural blanks, matching sample
164 gas extractions precisely but without firing the laser, were run every four analyses. The
165 Noblesse instrument has sufficiently high resolution to distinguish an almost entirely
166 hydrocarbon free shoulder at mass 36, where the measurement for ^{36}Ar is made. For further
167 details of the analytical procedures refer to Deino et al. (2010). Interference corrections for
168 all data are after Renne et al. (2015) and are included in the **Data Repository 3**.

169 1.2.3 Integrating the ^{40}Ar/^{39}Ar data

170 ^{40}Ar/^{39}Ar ages, including *R*-values are presented in **Table S3**. Individual probability diagrams
171 are presented below in **Figures S3-6**. The overall rank order of all analyses used in
172 generated the fully integrated ^{40}Ar/^{39}Ar weighted mean age for the eruption deposit at Campi
173 Flegrei Caldera are presented in **Figure S7**. All measurements are provided in **Data**
174 **Repository 3**.

175 S-19 25.9-22.5 m (3rd eruption deposit above the Campanian Ignimbrite in S-19 borehole)

176 A total of twenty-four ^{40}Ar/^{39}Ar measurements for the S-19 sample 22.9 were made at LSCE.
177 The first seventeenth measures were obtained by the analyses on single grains while the

178 last seven others were done by the analyses of small crystal populations (two or three
179 crystals simultaneously fused). The results obtained present a clear bi-modal probability
180 diagram (**Fig. S3**) with two distinct populations. Both populations are homogeneous, with the
181 dominant younger population comprising eighteen of the twenty-four measurements made.
182 The $^{40}Ar/^{39}Ar$ weighted mean age determined for this upper portion of the eruption deposit is
183 29.0 ± 0.8 ka (2σ). A secondary population of ages cluster at ~40 ka, consistent with the age
184 of the large CI eruption (Giaccio et al., 2017), confirming them as a population of xenocrysts.
185 The 2 sigma age range of the CI xenocrysts identified in the S-19 22.9 m sample can be
186 used, in conjunction with the stratigraphic position of all investigated units above the CI, as a
187 basis to exclude CI xenocrysts from the remaining samples analysed. If the uncertainties of
188 individual analyses have been properly quantified and the tephra has been adequately
189 sampled, we expect a single population of data representing one event to yield MSWD = 1.
190 Uncertainties increase if gas yields are low and the blank correction becomes significant
191 compared to the gas measurement, as is expected with young samples and/or smaller grain
192 sizes. Removing the CI-age grains yields MSWD < 1 for each BGC data set due to 1σ
193 uncertainties of individual analyses ranging from ~1-10 ka, but removal also results in
194 probability (P) ~ 1 and the results agree with geologic/stratigraphic information necessitating
195 the exclusion of those grains. Fifty-nine sanidine crystals from the S-19 borehole sample
196 25.8 m (post-CI Unit 3) analysed at BGC (Nexus), fifty-seven of which present a unimodal
197 probability distribution (**Fig. S4**). However, considering the higher precision dating of the
198 upper portion of eruption deposit (Sample 22.9 m), thirteen of the fifty-seven crystals can be
199 interpreted as CI xenocrysts and removed from the age computation. The $^{40}Ar/^{39}Ar$ weighted
200 mean age for the basal portion of the post-CI Unit 3 in the S-19 core is 28.4 ± 2.1 ka (2σ)
201 (MSWD = 0.52, P=1, n=44). The combined $^{40}Ar/^{39}Ar$ weighted mean age for the S-19 25.9-
202 22.5 m eruption deposit is 29.0 ± 0.8 ka (2σ).

203 Ponti Rossi- CF132 age (4th eruption deposit above the Campanian Ignimbrite at Ponti
204 Rossi)

205 Two independent ages were produced for the upper portion of Ponti Rossi eruption deposit
206 (sample CF132). Thirty-two sanidine crystals were analysed at BGC using Nexus
207 instrument, thirty-one of which present a uni-modal probability distribution (**Fig. S5**). Eight of
208 thirty-one crystals were removed based on our stratigraphic and geochemical correlations of
209 this eruption deposit to the more precisely dated tephra in the S-19 borehole (sample 22.9
210 m) which clearly resolves the CI xenocrystic material. The $^{40}Ar/^{39}Ar$ weighted mean age of
211 the Ponti Rossi CF132 sample using Nexus is 31.6 ± 2.8 ka (MSWD = 0.33, P =1, n= 23).
212 Eighteen sanidine crystals analysed at BGC using the Noblesse instrument, fifteen of which
213 present a uni-modal density distribution (**Fig. S6**). Four of the fifteen crystals were removed
214 as Campanian Ignimbrite xenocryst as for reasons previously outlined for the Nexus analysis
215 of the sample. The $^{40}Ar/^{39}Ar$ weighted mean age of the Ponti Rossi CF132 sample using
216 Noblesse is 31.3 ± 2.6 ka (MSWD = 0.15, P = 1.0, n = 11), indistinguishable from the results
217 produced using Nexus. The combined $^{40}Ar/^{39}Ar$ weighted mean age for the CF132 is 31.4 ±
218 1.9 ka (2σ).

219 Integrated CFc near-source ($^{40}Ar/^{39}Ar$) geochronology

220 The $^{40}Ar/^{39}Ar$ weighted mean age of the Ponti Ro-CF131/132 (31.4 ± 1.9 ka) and of S-19
221 (29.0 ± 0.8 ka) eruption deposits are statistically indistinguishable at the 95.4% confidence
222 limit, even if their respective uncertainties differ largely in magnitude (**Table S3**). This is due

223 to the difference in how each laboratory imposes blank corrections on the samples. CNRS-
224 LSCE applies a bracketing blank correction which imposes the analytical uncertainty only
225 from the blanks run before and after the unknown analysis, while BGC imposes a mean
226 blank correction with a standard deviation from many (or all) blanks run over the course of
227 the total number of analyses of a sample. The latter approach is a more conservative
228 application of a blank correction in that it captures the variability among the blanks
229 themselves, resulting in a larger error contribution from the blank correction imposed on the
230 unknown and a larger uncertainty on the final age of a sample. The overall agreement in
231 age, coupled with the robust stratigraphic and geochemical correlation, allow us to combine
232 the ages of the near-source units (Ponti Rossi CF131-132 and S-19 25.9-22.5m). The
233 combined rank-order distribution of all the analysed grains used from CNRS-LSCE and BGC
234 to generate the ^{40}Ar/^{39}Ar weighted mean age of the eruption are presented in S. Figure 6.
235 The ^{40}Ar/^{39}Ar weighted mean age for this eruption at CFc of 29.34 ± 0.71 ka (2.σ).

236 **1.3 Ash dispersal modelling**

237 Ash dispersal associated with the Y-3 tephra deposits originating from CFc were simulated
238 using the HAZMAP model, which solves equations for advection, diffusion and
239 sedimentation of particles in two dimensions (Macedonio et al., 2005). This model assumes
240 that atmospheric dispersion of particles through wind transport and effective turbulent
241 diffusion, with fallout being controlled by terminal settling velocity (Macedonio et al., 2005).
242 Isopach maps were generated by modelling the tephra deposition in terms of mass loading
243 (kg m^{-2}) and converting to thicknesses, using a bulk density of 1000 kg m^{-3}, similar to other
244 Campanian eruption deposits (Costa et al., 2009).

245 Input parameters required for the dispersal model include: total erupted mass, eruption
246 column height, mass distribution along the column, total grain-size distribution (TGSD), wind
247 profile, and effective horizontal diffusion coefficient. As there is no direct way to estimate all
248 these parameters pertaining to the time of the eruptions, they were reconstructed by best
249 fitting observations of tephra thickness through minimizing the difference between observed
250 and modelled thickness (Costa et al., 2009; Matthews et al., 2012) using the equation:

$$S^2 = \sum_{i=1}^{N} w_i \left[T_i(obs) - T_i(calc) \right]^2$$

251 (S.1)

252 Where N is the number of data points (sample localities), w_i is the weighting factor, and
253 $T_i(obs)$ and $T_i(calc)$ represent the observed and calculated thicknesses, respectively.
254 Weighting factors depend on the distribution of random errors in the dependant variable. All
255 values have the same weight when $w_i = 1$ is used, and when $w_i = 1/T^2_i(obs)$ is used the
256 relative squared errors are minimised (i.e., proportional weighting). The use of $w_i = 1/T_i(obs)$
257 is a compromise between the minimising absolute and relative squared errors. In addition to
258 the above equation, as in Costa et al. (2014) and Poret et al. (2017), we computed the
259 statistical indexes K (i.e. geometric average of the distribution) and k (i.e. geometric standard
260 deviation of the distribution) that were introduced by Aida (1978) (see **Table S4**):

261 $$K = exp\left[\frac{1}{N}\sum_{i}^{N} \log\left(\frac{T_i(obs)}{T_i(calc)}\right)\right]; \quad k = exp\left[\sqrt{\frac{1}{N}\sum_{i}^{N} \log\left(\frac{T_i(obs)}{T_i(calc)}\right)^2 - \left(\frac{1}{N}\sum_{i}^{N} \log\left(\frac{T_i(obs)}{T_i(calc)}\right)\right)^2}\right]$$ (S.2)

262 In the model, the total erupted mass was calculated analytically to minimise the difference
263 between the modelled and observed layer thicknesses, optimizing either the relative error
264 (S.1) (proportional weighting) or the Aida indices (S.2). The column height was assessed in
265 the range of 30-60 km and was trailed in 1 km steps. The model assumes deposition was
266 from a filiform eruption column extending from a source area within CFc and an effective
267 average wind field across the region. The other parameters and the explored ranges are
268 reported in **Table S4**. There were six granulometric size classes assumed in the eruption
269 source parameters, with five representing particles falling as single particles and, following
270 Cornell et al. (1983), the last representing aggregates formed of fine particles (or single
271 particles having an equivalent settling velocity). Owing to a lack of available grain size
272 information to allow the TGSD to be reconstructed, we adopted information from the well-
273 studied deposits of the Campanian Ignimbrite eruption (**Table S5**, Marti et al., 2016). With
274 respect to the parameterization proposed by Cornell et al. (1983), which accounts for the
275 effects of ash aggregation, we assumed that all particles smaller or equal to 62 microns fall
276 as aggregates class with diameters of 200 microns (as in Cornell et al., 1983) (**Table S6**).
277 The Y-3 tephra is found but relatively confined, which suggests efficient aggregation and
278 supports the assumption that the small particles (62 microns) fell as aggregates.

279 It is important noting that the diverse eruption source parameter combinations and the inter-
280 dependency of input parameters used in the tephra dispersal model means the best-fit
281 solution is not unique (e.g., Bonasia et al., 2010; Connor & Connor, 2006; Marti et al., 2016).
282 Furthermore, the lack of detailed granulometry data to reconstruct the TGSD for the deposits
283 introduces large uncertainties. However, our sensitivity tests indicate that the total erupted
284 mass is in the range of 10-30 km^3 DRE and the plume height was between 40 and 60 km.
285 For a more information on the approach employed to model the tephra dispersal and its
286 limitations refer to Costa et al. (2009) and Matthews et al. (2012).

Table S1: Localities of Masseria del Monte Tuff and distal Y-3 tephra fall deposit thicknesses incorporated into the HAZMAP ash dispersal model. Proximal and medial (SMP1e) PDC unit thicknesses are incorporated in the volume estimate using the methods of Macedonio and Pareschi (1991). *At PR 10 cm of moderately-sorted pumice lapilli fall and 30 cm of ash fall. **In S-19, 5 cm moderately-sorted pumice fall lapilli fall and 5 cm of ash fall. ***active marine canyon, assumed to be flow deposits. ****Thickness for the simulations was assumed equal to 1 mm. ^Layer thickness not available. Also listed are distal visible and cryptotephra occurrences of the NYT used in Figure 1.

Site	Sequence (tephra)	Latitude	Longitude	Thickness (cm) Fall	PDC	Reference
Masseria del Monte /Y-3 tephra						
Ponti Rossi (PR)	CF131-132	40.877	14.265	40*	50	This study
S-19 Borehole (Naples)	25.9-22.5m	40.883	14.251	10**	330	This study
Sorrentine Peninsula	SMP1-e	40.686	14.465	-	45	Sulpizio et al.,2003; Zanchetta et al., 2008
Sorrentine Peninsula	SMP1-e	40.768	14.654	-	100	Di Vito et al., 2008; Zanchetta et al., 2008
Lago Grande di Monticchio	TM-15	40.931	15.604	28.6	-	Wulf et al., 2004
San Gregorio Magno Basin	S-19	40.655	15.423	15	-	Munno and Petrosino, 2007
Lake Ohrid (OH-DP)	OH-DP-115	41.051	20.718	1.5	-	Leicher et al., 2015
Lake Ohrid (Co1202)	OT0702-4	41.088	20.78	3	-	Vogel et al., 2010
Lake Ohrid (Lz1120)	896-897	40.938	20.758	1	-	Wagner et al., 2008
Lake Ohrid (Jo-2004)	Jo-187	40.92	20.699	3	-	Caron et al., 2010
Lake Prespa (Co1215)	PT0915-05	40.993	20.995	1	-	Damaschke et al., 2013
Tenaghi Philippon (Greece)	TP2005 9.70m	40.968	24.25	Cryptotephra****	-	Albert et al., 2015; Wulf et al., 2018
Tyrrhenian Sea (KET-80-11)	205cm (C-7)	39.406	15.072	1	-	Paterne et al., 1988
Tyrrhenian Sea (KET-80-04)***	264-274 (C-7)	39.828	13.875	-	10***	Paterne et al., 1988
Adriatic Sea (MD90-917)^	920-17	41.17	17.37	-	-	Zanchetta et al., 2008
Tyrrhenian Sea (Core_C-106)	565-579cm	40.463	14.738	14	-	Munno and Petrosino, 2004
Ionian Sea	RC9-191(245-244) (Y-3)	38.249	17.993	1	-	Keller et al., 1978
Ionian Sea	M25/4-12(245-244) (Y-3)	37.964	18.274	1	-	Kraml, 1997; Albert et al., 2015
Ionian Sea	M25/4-13 (Y-3)	37.496	17.667	1	-	Kraml, 1997; Albert et al., 2015
Distal Neapolitan Yellow Tuff						
PAL94-77 (+others)	550	42.25	15.05	-	-	Calanchi et al., 1998
CM92-42	200	42.37	15.12	-	-	Calanchi et al., 1998
RF95-12	560			-	-	Calanchi et al., 2008
IN68-9	225			-	-	Calanchi et al., 2008

Lake Fucino	TF-2	41.98	13.55	3	-	Giaccio et al., 2017
Lago Grande di Monticchio	TM-8	40.931	15.604	2.2	-	Wulf et al., 2004
San Gregorio Magno Basin	S-19	40.655	15.423	80	-	Munno and Petrosino, 2007
Adriatic Sea (MD90-917)	395	41.17	17.378	-	-	Siani et al., 2004
Adriatic Sea (KET-80-22)	155	41.44	17.37	-	-	Paterne et al., 1988
Tyrrhenian Sea (KET-80-04)***	115 cm (C-2)	39.828	13.875	-	-	Paterne et al., 1988
Lake Bled (Slovenia)	Bld_T240	46.36	14.09	cryptotephra	-	Lane et al., 2011
Adriatic Sea (PRAD1-2)	PRAD-218	42.40	14.46	cryptotephra	-	Bourne et al., 2010
Langsee (Austria)	369.5	46.78	14.43	cryptotephra	-	Schmidt et al., 2002

Table S2: Representative major and trace element volcanic glass analyses of near-source eruptive products form the S-19 borehole (25.9-22.5m) and the Ponti Rossi outcrop (CF131/132) considered here equivalent to the distal Y-3 Mediterranean Tephrostratigraphic marker. Also given are representative average data from the two dominant glass populations of the Y-3 tephra from its type locality in the Ionian Sea (Albert et al., 2015). Full data sets are given in DR2.

Sample	S-19						Ponti Rossi					Y-3 Ionian Sea			
Core/Locality	S-19-25.8m			S-19-22.9m			CF131			CF132		(M25/4-12; Albert et al., 2015)			
Sample I.D	29D	19C	14B	14B	24C	9B	22D	13C	1A	4A		Average	(2 s.d)	Average	(2 s.d)
Component	1	2	3	1	2	mixing	1	3	mixing	1	2	1		2	
Major, minor												(n=12)		(n=17)	
SiO$_2$	62.45	60.46	59.75	62.05	60.70	61.92	62.67	60.98	61.18	62.27	60.41	62.41	0.65	60.58	0.53
TiO$_2$	0.44	0.37	0.50	0.30	0.42	0.31	0.38	0.43	0.37	0.41	0.36	0.37	0.08	0.38	0.05
Al$_2$O$_3$	18.26	18.68	18.45	18.16	18.73	18.25	18.02	18.06	18.28	18.14	18.60	17.97	0.32	18.42	0.20
FeOt	2.82	3.54	3.72	2.95	3.29	3.02	2.66	3.43	3.34	2.83	3.60	2.86	0.18	3.53	0.34
MnO	0.14	0.06	0.13	0.15	0.07	0.15	0.12	0.11	0.20	0.13	0.10	0.14	0.07	0.10	0.11
MgO	0.41	0.77	0.98	0.32	0.63	0.49	0.39	0.85	0.57	0.37	0.76	0.40	0.10	0.78	0.11
CaO	2.11	2.53	3.29	2.14	2.46	2.26	1.93	2.92	2.36	2.11	2.65	2.14	0.18	2.64	0.24
Na$_2$O	4.13	2.88	4.12	4.48	3.15	3.91	4.66	4.02	3.78	4.26	2.64	4.39	0.42	3.12	0.28
K$_2$O	8.40	10.10	7.99	8.42	9.93	8.96	8.31	8.20	9.14	8.62	10.33	8.54	0.35	9.96	0.28
P$_2$O$_5$	0.04	0.18	0.22	0.07	0.15	0.04	0.06	0.18	0.13	0.05	0.17	0.07	0.05	0.14	0.04
Cl	0.81	0.43	0.86	0.97	0.47	0.68	0.82	0.82	0.63	0.82	0.39	0.72	0.11	0.35	0.07
Analytical Total	96.35	95.71	98.41	96.68	97.34	94.90	94.54	98.21	98.17	94.66	95.14	95.90		96.68	
Trace															
Rb	330	297	344	329	256	310	351	333	327	364	280	345	*10*	273	10
Sr	130	534	369	181	463	269	116	330	281	139	574	137	11	558	106
Y	32	20	28	30	19	24	30	29	24	32	19	31	2	20	2
Zr	380	182	326	357	181	277	370	336	273	395	173	368	23	190	32
Nb	61	31	49	52	29	44	59	57	48	60	30	54	3	31	7
Ba	22	647	340	58	568	137	18	314	172	25	830	26	8	703	194
La	72	46	66	72	43	57	73	69	60	78	46	69	3	45	4
Ce	152	91	123	133	85	110	140	131	107	153	82	133	5	86	11
Pr	14.4	9.7	13.6	14.6	9.1	11.0	13.7	14.5	11.1	15.1	9.3	13.6	0.8	9.1	1.2
Nd	49.7	32.7	44.8	47.2	32.4	39.4	47.6	50.2	39.6	51.2	31.6	49.7	4.7	34.4	4.9
Sm	9.4	6.5	9.0	9.4	5.9	7.6	8.5	9.4	7.4	9.3	5.8	8.9	1.3	6.2	1.6
Eu	1.8	2.0	1.7	-	1.9	1.9	1.6	1.7	1.6	1.6	1.9	1.6	0.2	1.9	0.4
Gd	6.8	4.9	6.9	7.3	4.5	5.7	6.8	6.4	5.7	7.4	4.0	6.7	1.7	4.9	0.7
Dy	6.0	3.9	5.3	5.4	3.9	4.2	5.6	5.7	4.9	6.0	3.9	5.7	0.6	4.1	0.9
Er	3.0	2.0	2.9	3.4	1.8	2.4	3.0	3.2	2.3	3.2	1.8	3.1	0.2	2.0	0.4
Yb	3.4	1.9	2.5	2.8	1.9	-	3.4	-	-	3.4	-	3.1	0.4	1.8	0.4
Ta	2.7	1.4	2.4	2.8	1.3	2.1	2.7	2.8	2.1	2.9	1.3	2.8	0.3	1.5	0.4
Th	33.1	15.5	29.8	31.4	14.3	24.6	31.6	29.9	23.5	32.9	13.4	30.9	2.4	14.5	2.3
U	11.6	5.0	10.6	11.0	5.3	9.3	11.7	10.6	9.1	11.6	4.6	10.2	0.9	4.9	1.1
Nb/Th	1.8	2.0	1.6	1.7	2.0	1.8	1.9	1.9	2.0	1.8	2.3	1.8	0.1	2.1	0.2
Zr/Th	11.5	11.8	10.9	11.4	12.7	11.3	11.7	11.2	11.6	12.0	12.9	11.9	0.5	13.1	0.6
Nb/Zr	0.16	0.17	0.15	0.15	0.16	0.16	0.16	0.17	0.18	0.15	0.17	0.15	0.01	0.16	0.02

Table S3: Calculated $^{40}Ar/^{39}Ar$ ages and R-values for Tufi Biancastri deposits at Ponti Rossi (PR) sample CF-132, and S-19 borehole samples 25.8 and 22.9 m considered the near-source counterpart of the Y-3 tephra. Integrated $^{40}Ar/^{39}Ar$ weighted mean eruption age. Ages calculated with the air correction after Lee et al (2006), the ACs fluence monitor age of 1.1891 Ma (Niespolo et al., 2017) and the decay constants of Renne et al. (2011).

Sample	Mass Spec	Lab ID	R^{Y-3}_{ACs}	± (1σ)	R^{Y-3}_{FCs}	± (1σ)	Age, ka	± (2σ), ka	n/N
PR - CF 132	Noblesse	37163	0.026279	0.001107	0.001096	4.623E-05	31.25	2.64	11 / 18
PR - CF 132	Nexus	37163	0.026568	0.001156	0.001108	4.8286E-05	31.60	2.75	23 / 32
Core S19 - 25.8m	Nexus	37157	0.023888	0.000866	0.000996	3.6179E-05	28.41	2.06	44 / 63
Core S19 - 22.9m	VG 5400	N1530/ N1539	0.024464	0.000337	0.001020	1.4045E-05	29.00	0.80	18 / 24
Masseria del Monte Tuff/ Y-3 tephra - weighted mean			**0.024659**	**0.000292**	**0.001028**	**1.22E-05**	**29.34**	**0.71**	**96 / 137**

Table S4: Results of the HAZMAP tephra dispersal modelling of the Masseria del Monte Tuff/Y-3 tephra from Campi Flegrei caldera. The values in brackets are the steps used in the model to assess the best-fit scenario.

Modelled dispersal parameters	Explored range (step)	Y-3 tephra
Fallout volume (DRE; km^3)	Calculated	16
Fallout mass (kg)	Calculated	4.5×10^{13}
Wind velocity (m/s)	1 to 50 (1)	12
Wind azimuth (o clockwise from North)	0 to 360 (1)	348
Column Height (H, km)	30 to 60 (1)	59
Suzuki Coefficient	1 to 9 (1)	7
Diffusion coefficient (K, m^2/s)	5000 to 80,000 (5000)	70,000
Deposit Density	Assumed to be similar to CI (1000)	
TGSD	Assumed to be similar to CI co-ignimbrite phase (Marti et al., 2016), with all particles $<$/$=$ 62 μm in diameter settling as aggregates with diameters of 200 μm.	

Table S5. TGSD of the co-ignimbrite/co-PDC phase of the Campanian Ignimbrite (Marti et al., 2016).

Φ	%
-1	0.37
0	1.45
1	1.80
2	3.05
3	8.50
4	17.90
5	24.17
6	20.77
7	12.66
8	6.36
9	2.28
10	0.68

Table S6. Effective TGSD used in the simulations. The aggregate density was estimated by the model, which explored a range of values (100 to 1500 kg/m^3). Particle terminal settling velocities were calculated according to Ganser (1993).

Particle diameter (Φ)	Particle density (kg/m^3)	Particle sphericity (-)	%
-1	500	0.85	0.37
0	725	0.85	1.45
1	950	0.85	1.80
2	1175	0.85	3.05
3	1400	0.85	8.50
Aggregate: Φ=2.3 (200 μm)	1000	1.00	84.83

Table S7. Observed vs simulated deposit thicknesses at the different locations, for locations please refer to Table S1.

Locations	Observed deposit (cm)	Simulated deposit (cm) from best K and k values	Simulated deposit (cm) from best σ^2 value
Ponti R_	40	24.55	19.09
S-19	10	24.05	18.70
Tenaghi Philippon	0.1	0.11	0.08
LGdM	28.6	31.08	24.17
OH-DP-	1.5	1.80	1.40
Co1202	3	1.59	1.24
Lz1120	1	2.05	1.59
JO-200	3	2.20	1.71
PT0915	1	1.61	1.26
SGMB	15	38.06	29.59
Core_C	14	25.18	19.58
KET_80	1	1.69	1.32
M25-12	1	0.44	0.35
M25-13	1	0.04	0.03
RC9-19	1	1.40	1.09
Statistical indices		$K = 1.04; k = 2.67$	$\sigma^2 = 0.31$
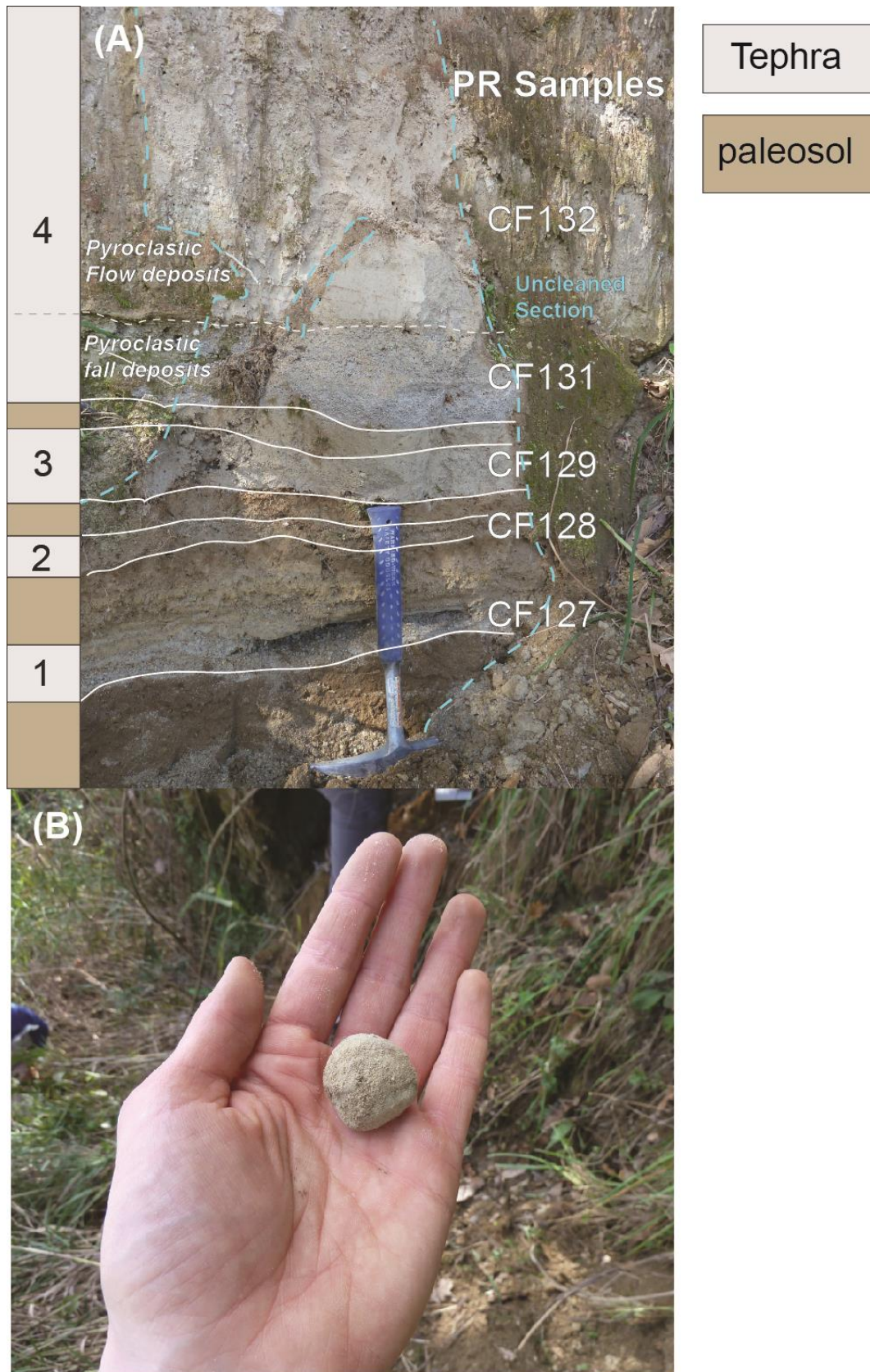
Figure S1: (A) The Ponti Rossi succession comprising of alternating tephra units and palaeosols, the thickest Tufi Biancastri unit (fourth unit; CF131-132), has (B) large accretionary lapilli in the upper PDC deposits (sample CF132) and is correlated to the thickest unit in the S-19 borehole, which are both in turned correlated to the distal Y-3 tephra.
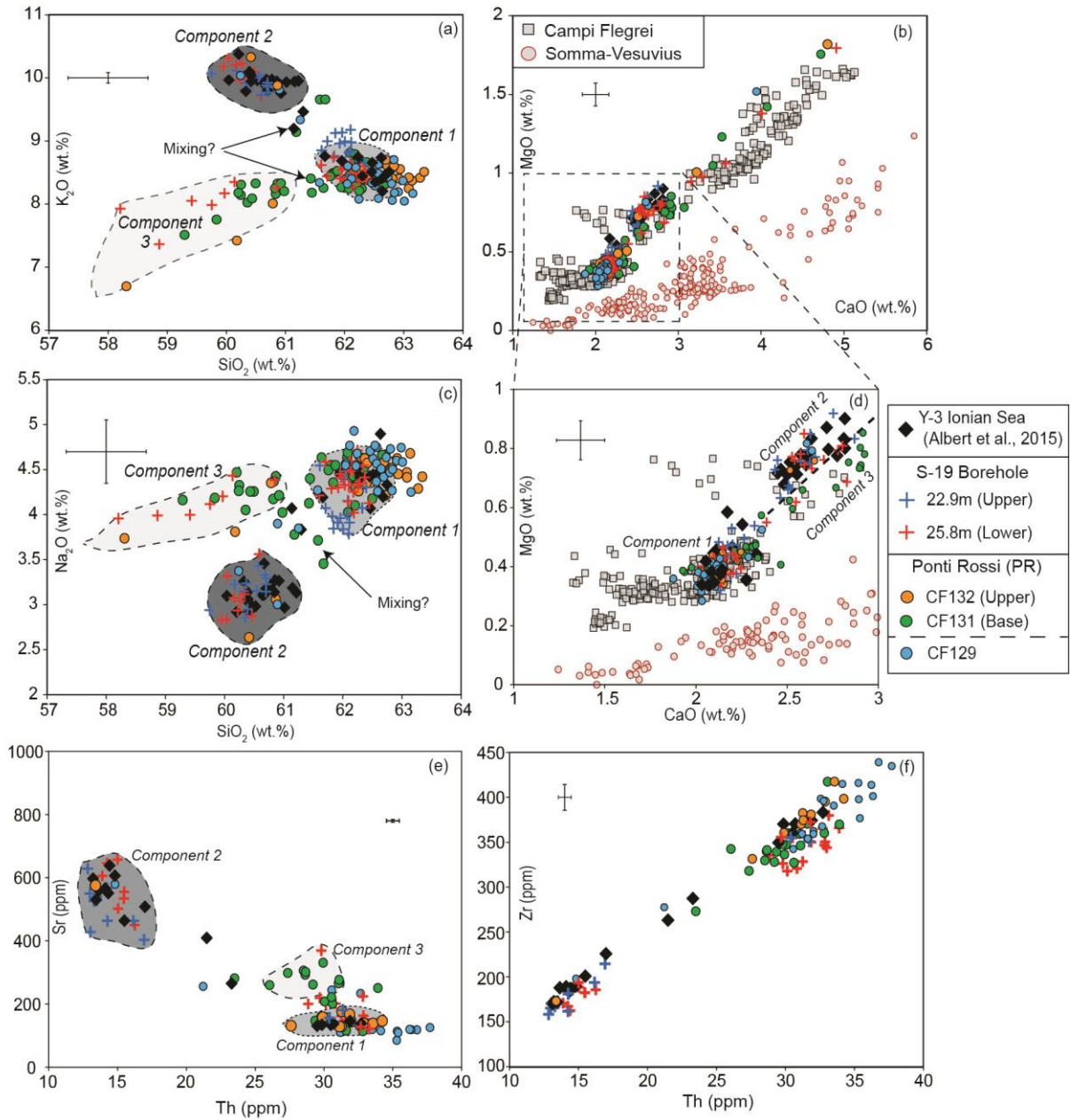
Figure S2: Selected major and trace element bi-plots illustrating the chemical correlation between the volcanic glasses of the Y-3 and the Ponti Rossi tephra (CF131/132) and borehole tephra (S-19 25.9-22.5m). (a-d) These bi-plots highlight the three compositional groupings referred to in the text. (e-f) highlight that the thin ash unit (CF129) at Ponti Rossi underlying the thickest tephra (CF131/132) extend to more elevated level of enrichment in incompatible trace elements than those observed in the distal Y-3 tephra.
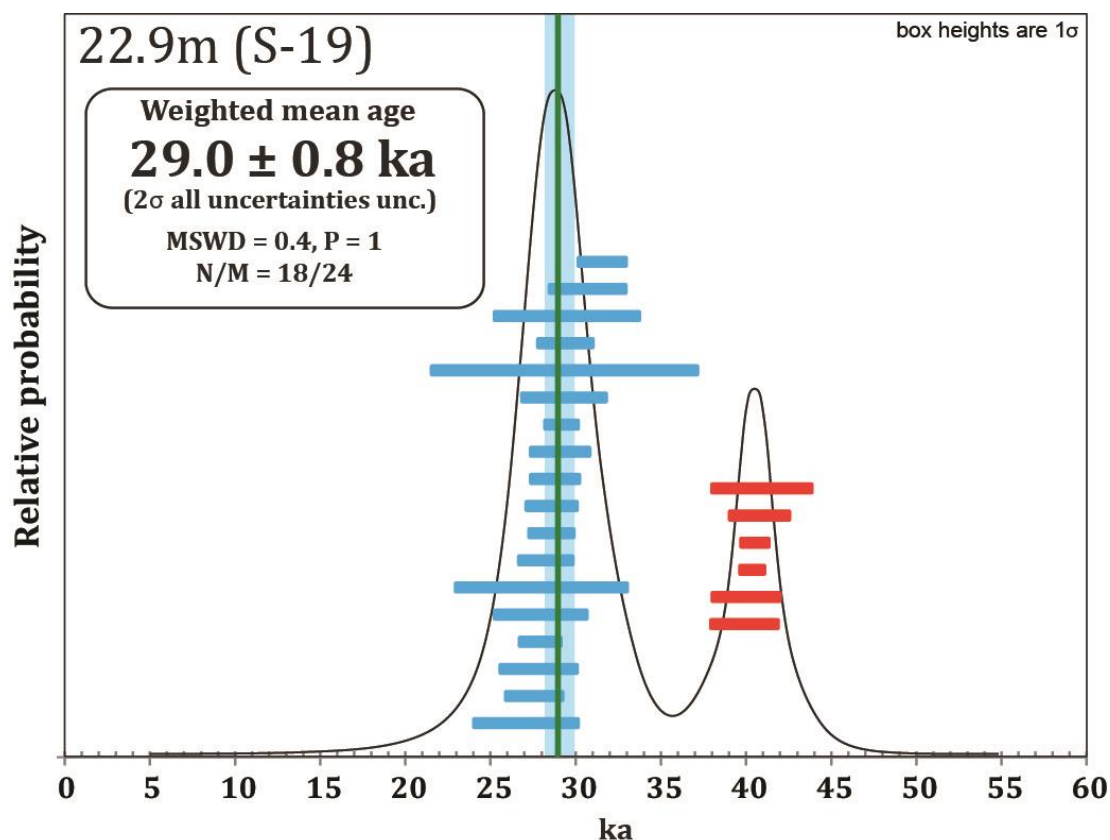
Figure S3: Bi-modal probability of the sample S19-22.9m sample analysed at LSCE and its $^{40}Ar/^{39}Ar$ weighted mean age. Age generated excludes the 40 ka Campanian Ignimbrite xenocrysts population (red; see text)
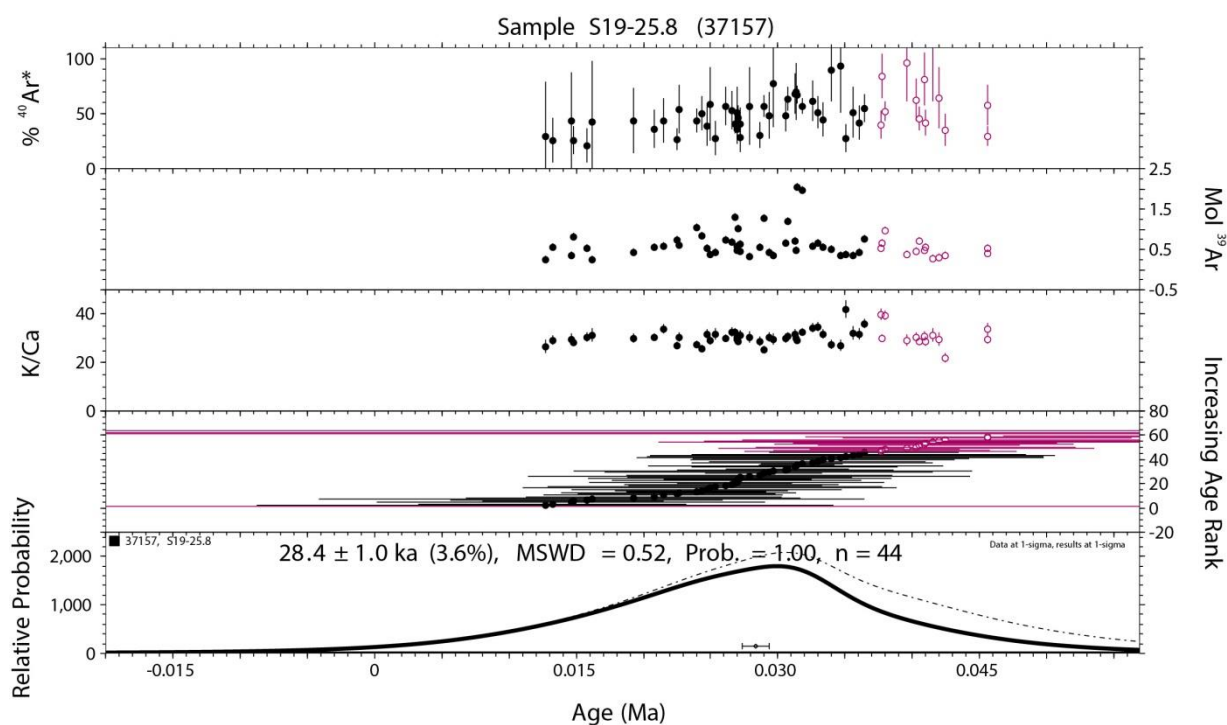
Figure S4: Unimodal probability distribution of sample S-19 25.8m and $^{40}Ar/^{39}Ar$ weighted mean age for sample S19-22.9m sample analysed using Nexus at BGC. Pink analyses were removed as Campanian Ignimbrite xenocrysts (See text above).
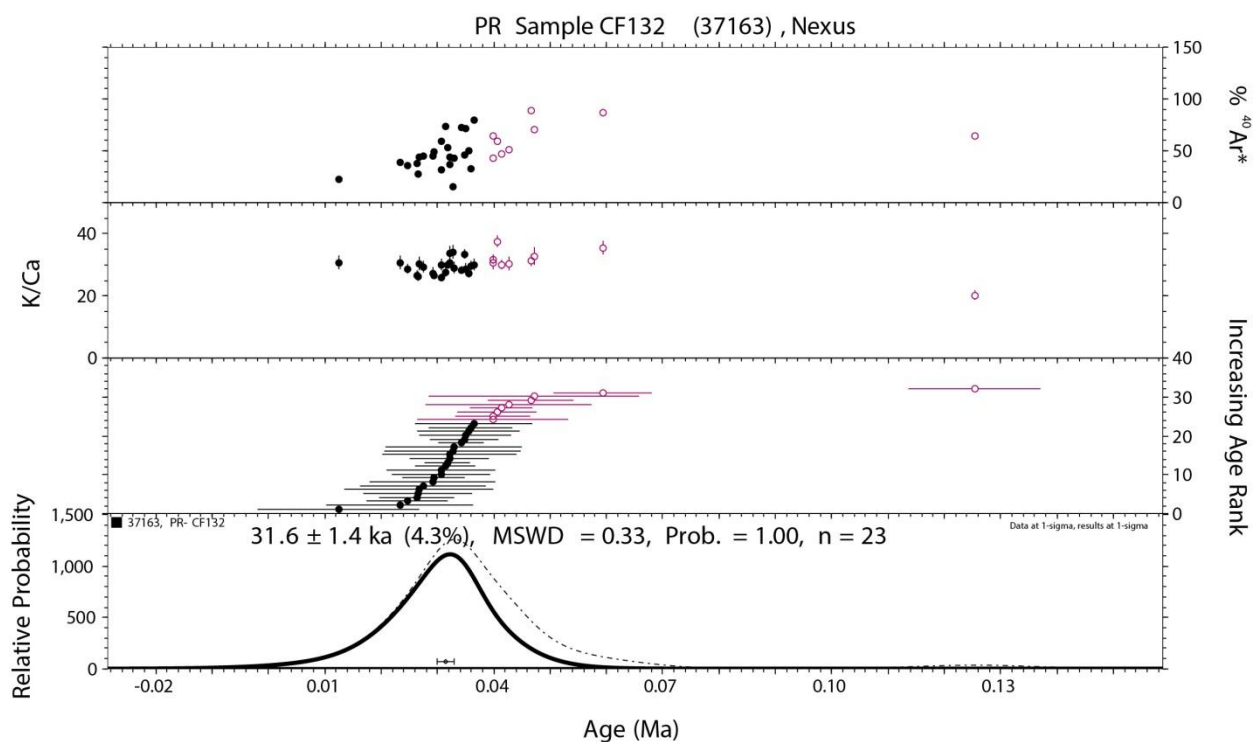
Figure S5: Unimodal probability distribution of sample S-19 25.8m and ^{40}Ar/^{39}Ar weighted mean age for the Ponti Rossi sample CF132 sample analysed using Nexus at BGC. Pink analyses were removed as Campanian Ignimbrite xenocrysts (See text above).
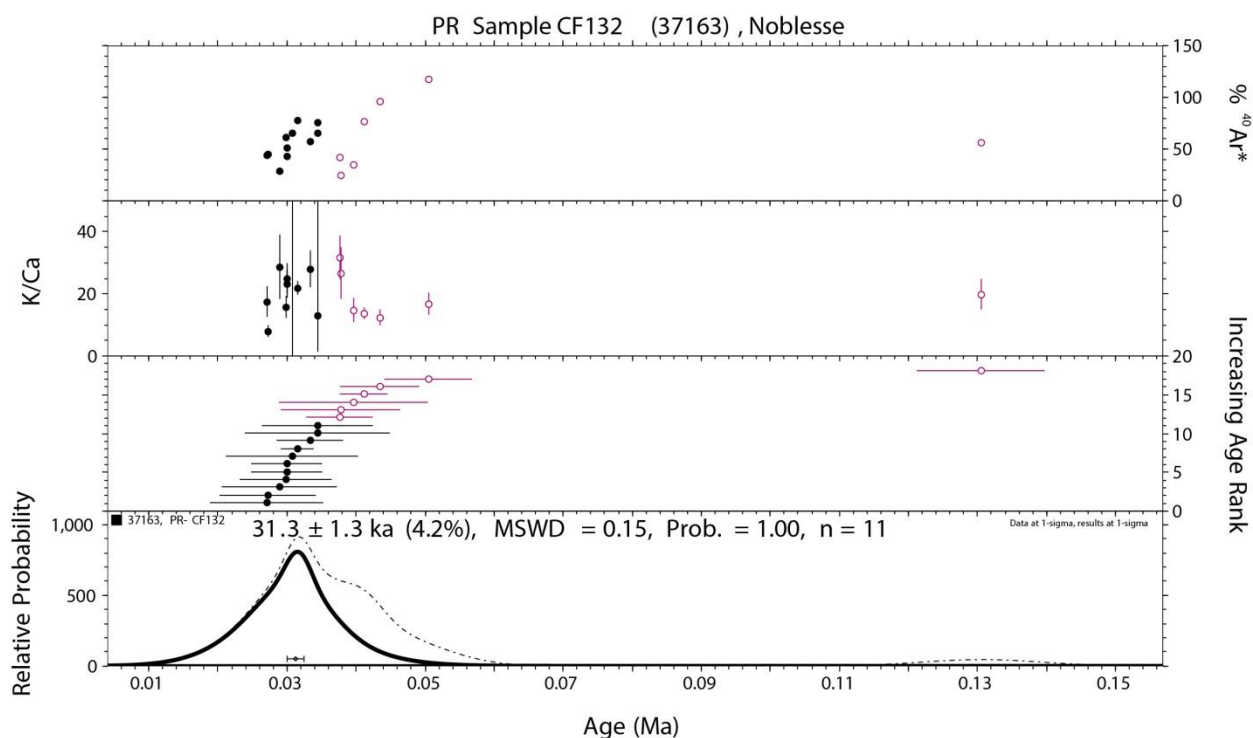
Figure S6: Unimodal probability distribution of sample S-19 25.8m and ^{40}Ar/^{39}Ar weighted mean age for the Ponti Rossi sample CF132 sample analysed using Noblesse at BGC. Pink analyses were removed as Campanian Ignimbrite xenocrysts (See text above).
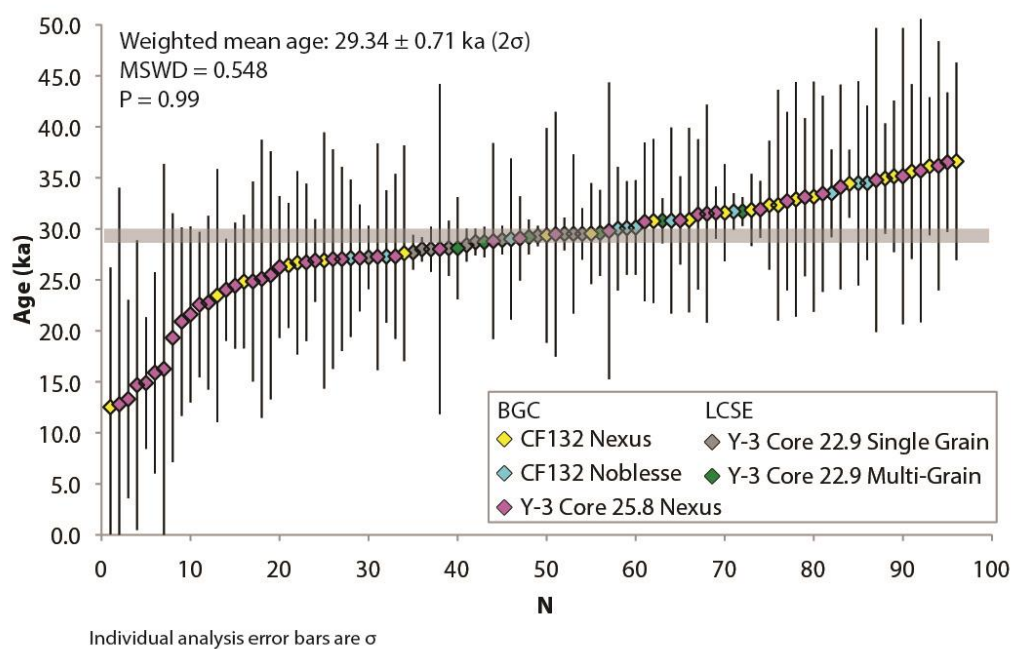
Figure S7: Rank order diagram combining all age determinations used to produce the final integrated $^{40}Ar/^{39}Ar$ weighted mean age of the Masseria del Monte Tuff/Y-3.
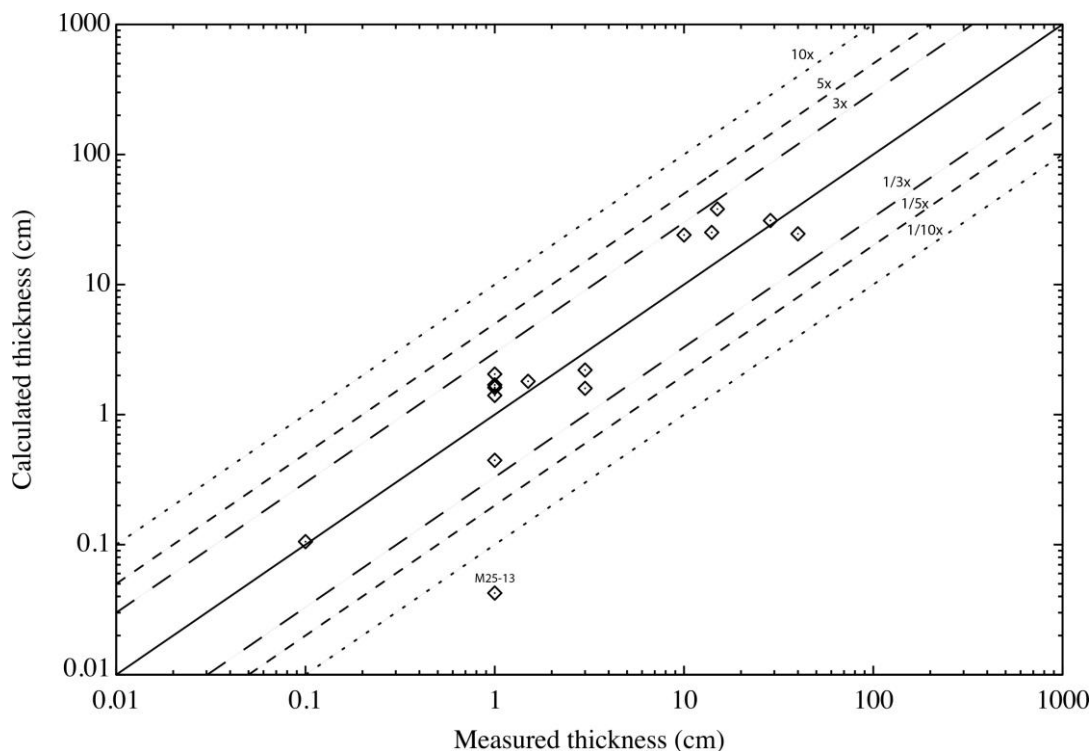
Figure S8: Comparison between the HAZMAP simulation of the Y-3 ash dispersal across the Central and Eastern Mediterranean using values obtained by best-fit procedures of tephra thickness at each sampling point. Localities and layer thickness incorporated into the HAZMAP model are presented in Supplementary Table 1, along with the explored eruption parameters in Supplementary Table 4. The equiline (black solid line) represents the ideal fit if perfect agreement can be achieved, most points lie in the region between 3 and 1/3 times.

Supplementary References

Aida, I. (1978). Reliability of a tsunami source model derived from fault parameters. *J. Phys. Earth* 26, 57–73

Albert, P.G., Hardiman, M., Keller, J, Tomlinson, E.L., Bourne, A, J., Smith, V.C. Wulf, S., Zanchetta, G., Sulpizio, R., Müller, U.C., Pross, J., Ottolini, L., Matthews, I.P., Blockley, S.P., Menzies, M.A., 2015, The Y-3 tephrostratigraphic marker revisited: new diagnostic glass geochemistry, improved chronology and climatostratigraphic interpretations: Quaternary Science Reviews, 118, 105-121.

Bonasia, R., Macedonio, G., Costa, A., Mele, D., Sulpizio, R., 2010, Numerical inversion and analysis of tephra fallout deposits from the 472 AD sub-Plinian eruption at Vesuvius (Italy) through a new best-fit procedure: Journal of Volcanology and Geothermal Research 189, 238-246.

Bourne, A.J., Lowe, J.J., Trincardi, F., Asioli, A., Blockley, S.P.E., Wulf, S., Matthews, I.P., Piva, A., Vigliotti, L., 2010, Distal tephra record for the last ca 105,000 years from core PRAD 1-2 in the central Adriatic Sea: implications for marine tephrostratigraphy: Quaternary Science Reviews 29, 3079-3094.

Buccheri, G., Bertoldo, G., Coppa, M.G., Munno, R., Pennetta, M., Siani, G., Valente, A., Vecchione, C., 2002a. Studio multidisciplinare della successione sedimentaria tardo-quaternaria proveniente dalla scarpata continentale del Golfo di Policastro (Tirreno meridionale): Boll. Soc. Geol. It. 121, 187-210.

Calanchi, N., Dinelli, E., 2008, Tephrostratigraphy of the last 170 ka in sedimentary successions from the Adriatic Sea: Journal of Volcanology and Geothermal Research 177(1), 81-95.

Calanchi, N., Cattaneo, A., Dinelli, E., Gasparottoa, G., Lucchini, F., 1998. Tephra layers in Late Quaternary sediments of the central Adriatic Sea: Marine Geology 149 (1-4),191-209.

Connor, L. & Connor, C. Inversion is the Key to Dispersion: Understanding Eruption Dynamics by Inverting Tephra Fallout. *In: Statistics in Volcanology* (Special Publications of IAVCEI, 1. Geological Society, London, pp. 231–242, 2006).

Caron, B., Sulpizio, R., Zanchetta, G., Siani, G., Santacroce, R., 2010, The Late Holocene to Pleistocene tephrostratigraphic record of Lake Ohrid (Albania): Comptes Rendus Geoscience Volume 342, 6, 453-466.

Cornell, W., Carey, S., Sigurdsson, H., 1983. Computer simulation of transport and deposition of the Campanian Y-5 ash. Journal of Volcanology and Geothermal Research 17, 89-109.

Costa, A., Dell'Erba, F., Di Vito, M.A., Isaia, R., Macedonio, G., Orsi, G., Pfeiffer, T., 2009. Tephra fallout hazard assessment at the Campi Flegrei caldera (Italy). Bulletin of Volcanology 71 (3), 259-273.

Damaschke, M., Sulpizio, R., Zanchetta, G., Wagner, B., Böhm, A., Nowaczyk, N., Rethemeyer, J., Hilgers, A., 2013. Tephrostratigraphic studies on a sediment core from Lake Prespa in the Balkans. Climate of the Past 9, 267-287

Deino, A.L., Scott, G.R., Saylor, B., Alene, M., Angelini, J.D., Haile-Selassie, Y., 2010. 40Ar/39Ar dating, paleomagnetism, and tephrochemistry of Pliocene strata of the hominid-bearing Woraso-Mille area, west-central Afar Rift, Ethiopia. Journal of Human Evolution 58, 111-126.

Di Vito, M.A., Sulpizio, R., Zanchetta, G., D'Orazio. 2008. The late Pleistocene pyroclastic deposits of the Campanian plain: New insights into the explosive activity of the Neapolitan volcanoes. Journal of Volcanology and Geothermal Research 177 (1), 19-48.

Ganser, G.H., 1993. A rational approach to drag prediction of spherical and non- spherical particles. Powder Technol. 77:143–152. https://doi.org/10.1016/0032- 5910(93)80051-B.

Giaccio, B., Hajdas, I., Isaia, R., Deino, A., Nomade, S., 2017. High-precision ^{14}C dating and ^{40}Ar/^{39}Ar dating of the Campanian Ignimbrite (Y-5) reconciles the time-scales of climatic-cultural processes at 40 ka. Scientific Reports 7, 45940. doi:10.1038/srep45940

Giaccio, B., Niespolo, E., Pereira, A., Nomade, S., Renne, P.E., Albert, P.G., Arienzo, I., Regattieri, E., Wagner, B., Zanchetta, G., Gaeta, M., Galli, P., Mannella, G., Peronace., E., Sottili, G., Florindo, F., Leicher, N., Marra, F., Tomlinson, E.L., 2017. First integrated tephrochronological record for the last ~190 kyr from the Fucino Quaternary lacustrine succession, central Italy. Quaternary Science Reviews 158, 211-234

Jochum, K.P., Stoll, B., Herwig, K., Willbold, M., Hofmann, A.W., Amini, M., Aarburg, S., Abouchami, W., Hellebrand, E., Mocek, B., Raczek, I., Stracke, A., Alard, O., Bouman, C., Becker, S., Dücking, M., Brätz, H., Klemd, R., de Bruin, D., Canil, D., Cornell, D., de Hoog, C., Dalpé, C., Danyushevsky, L., Eisenhauer, A., Gao, Y., Snow, J.E., Groschopf, N., Günther, D., Latkoczy, C., Guillong, M., Hauri, E., Höfer, H.E., Lahaye, Y., Horz, K., Jacob, D.E., Kasemann, S.A., Kent, A.J.R., Ludwig, T., Zack, T., Mason, P.R.D., Meixner, A., Rosner, M., Misawa, K., Nash, B.P., Pfänder, J., Premo, W.R., Sun, W.D., Tiepolo, M., Vannucci, R., Vennemann, T., Wayne, D., Woodhead, J.D., 2006. MPI-DING reference glasses for in situ microanalysis: 581 New reference values for element concentrations and isotope ratios. 582

Lane, C.S., Andric, M., Cullen, V.L., Blockley, S.P.E., 2011. The occurrence of the distal Icelandic and Italian tephra in the Lateglacial of Lake Bled, Slovenia. Quaternary Science Reviews 30(9-10), 1013-1018.

Lee, J.Y., Marti, K., Severinghaus, J.P., Kawamura, K., Yoo, H.-S., Lee, J.B., Kim, J.S., 2006. A redetermination of the isotopic abundances of atmospheric Ar. Geochimica et Cosmochimica Acta 70, 4507–4512.

Leicher, N., Zanchetta, G., Sulpizio, R., Giaccio, B., Wagner, B., Nomade, S., Francke, A., and Del Carlo, P. First tephrostratigraphic results of the DEEP site record from Lake Ohrid (Macedonia and Albania). Biogeosciences 13, 2151–2178, doi:10.5194/bg-13-2151-2016.

Macedonio, G., Costa, A., Longo, A., 2005. A computer model for volcanic ash fallout and assessment of subsequent hazard. Computers and Geoscience 31, 837-845.

Macedonio, G. and Pareschi, M.T., 1991. An algorithm for the triangulation of arbitrarily distributed points: Applications to volume estimates and terrain fitting. Comput. Geosci. 17, 859-874

Marti A., Folch A., Costa A., Engwell A. (2016) Reconstructing the plinian and co-ignimbrite sources of large volcanic eruptions: a novel approach for the Campanian Ignimbrite, Sci. Rep., 6, 21220, 1-11, doi:10.1038/srep21220

Mastin, L.G., Van Eaton, A.R., Durant, A.J., 2016. Adjusting particle-size distributions to ac- count for aggregation in tephra-deposit model forecasts. Atmos. Chem. Phys. 16: 9399–9420. https://doi.org/10.5194/acp-16-9399-2016.

Matthews, N.E., Smith, V.C., Costa, A., Durant, A.J., Pyle, D.M., Pearce, N.J.G., 2012. Ultra-distal tephra deposits from super-eruptions: Examples from Toba, Indonesia and Taupo Volcanic Zone, New Zealand. Quaternary International 258, 54-79.

Munno, R., Petrosino, P., 2004. New constraints on the occurrence of Y-3 Upper Pleistocene tephra marker layer in the Tyrrhenian Sea. Il Quaternario 17, 11-20.

Munno, R., Petrosino, P., 2007. The Late Quaternary tephrostratigraphical record of the San Gregorio Magno basin (southern Italy). Journal of Quaternary Science 22 (3), 247-266.

Mele, D., Dioguardi, F., Dellino, P., Isaia, R., Sulpizio, R., Braia, G., Hazard of pyroclastic density currents at the Campi Flegrei Caldera (Southern Italy) as deduced from the combined use of facies architecture, physical modeling and statistics of the impact parameters. Journal of Volcanology and Geothermal Research 299, 35-53.

Niespolo, E.M., Rutte, D., Deino, A.L., Renne, P.R., 2017. Intercalibration and Age of the Alder Creek 40Ar/39Ar standard. Quaternary Geochronology 39, 205-213.

Nomade, S., Renne, P.R., Vogel, N., Deino, A.L., Sharp, W.D., Becker, T.A., Jaouni, A.R., Mundil, R., 2005. Alder Creek sanidine (ACs-2): A Quaternary Ar-40/Ar-39 dating standard tied to the Cobb Mountain geomagnetic event. Chemical Geology 218, 315–338.

Paterne, M., Guichard, F., Labeyrie, J. 1988. Explosive activity of the South Italian volcanoes during the past 80,000 years as determined by marine tephrochronology. Journal of Volcanology and Geothermal Research 34, 153-172.

Poret, M., Costa, A., Folch, A., and Martì, A.: Modelling tephra dispersal and ash aggregation: The 26th April 1979 eruption, La Soufrière St. Vincent, J. Volcanol. Geotherm. Res., 347, 207–220, doi:10.1016/j.jvolgeores.2017.09.012

Renne, P.R., Balco, G., Ludwig, K.R., Mundil, R., Min, K., 2011. Response to the comment by W.H. Schwarz et al. on "Joint determination of 40K decay constants and 40Ar*/40K for the Fish Canyon sanidine standard, and improved accuracy for 40Ar/39Ar geochronology" by PR Renne, et al. (2010): Geochimica et Cosmochimica Acta 75, 5097-5100.

Renne, P.R., Sprain, C.J., Richards, M.A., Self, S., Vanderkluysen, L., Pande, K., 2015. State shift in Deccan volcanism at the Cretaceous-Paleogene boundary, possibly induced by impact: Science 350, 76-78.

Schmidt, R., Van Den Bogaard, C., Merkt, J., Muller, J., 2002, A new Lateglacial chronostratigraphic tephra marker for the southern-eastern Alps: the Neapolitan Yellow Tuff (NYT) in Langsee (Austria) in the context of a regional biostratigraphy and palaeoclimate: Quaternary International 88, 45-56.

Siani, G., Sulpizio, R., Paterne, M., Sbrana, A., 2004, Tephrostratigraphy study for the last 18,000 14C years in a deep-sea sediment sequence for the South Adriatic: Quaternary Science Reviews 23 (23-24), 2485-2500,

Smith, V.C., Isaia, R., Pearce, N.J.G., 2011, Tephrostratigraphy and glass compositions of post-15 kyr Campi Flegrei eruptions: implications for eruption history and chronostratigraphic markers: Quaternary Science reviews 30, 3638-3660.

Steiger, R.H., Jäger, E., 1977. Subcommission on geochronology: Convention on the use of decay constants in geo- and cosmochronology. Earth and Planetary Science Letters 36, 3, 359-362.

Sulpizio, R., Van Welden, A., Caron, B., Zanchetta, G., 2010. The Holocene tephrostratigraphic record of Lake Shkodra (Albania and Montenegro). Journal of Quaternary Science 25, 5, 633-650.

Sulpizio, R., Zanchetta, G., Paterne, M., Siani, G. 2003. A review of tephrostratigraphy in central and southern Italy during the last 65 ka. Il Quaternario 16, 91-108.

Wulf, S., Kraml, M., Brauer, A., Keller, J., Negendank, J.F.W., 2004. Tephrochronology of the 100 ka lacustrine sediment record of Lago Grande di Monticchio (southern Italy). *Quaternary International* 122, 7–30.

Zanchetta, G., Sulpizio, R., Giaccio, B., Siani, G., Paterne, M., Wulf, S. D'Orazio, M. 2008. The Y-3 tephra: A last glacial stratigraphic marker for the central Mediterranean basin. *Journal of Volcanology and Geothermal Research* 177(1), 145-154.